Nano Research
2022, 15(10): 8946–8954

ISSN 1998-0124 CN 11-5974/O4
https://doi.org/10.1007/s12274-022-4523-z

Enhancing Li-ion conduction and mechanical properties via addition of fluorine-containing metal–organic frameworks in all-solid-state cross-linked hyperbranched polymer electrolytes

Wen Wen[1,2,§], Qinghui Zeng[1,§], Pingping Chen[1], Xin Wen[1], Zhenfeng Li[1], Yu Liu[1], Jiazhu Guan[1], Anqi Chen[1], Wei Liu[1] (✉), and Liaoyun Zhang[1] (✉)

[1] School of chemical sciences, University of Chinese Academy of Sciences, Beijing 100049, China
[2] Research Institute of Petroleum Exploration & Development (RIPED), PetroChina, Beijing 100083, China
[§] Wen Wen and Qinghui Zeng contributed equally to this work.

Received: 10 March 2022 / **Revised:** 4 May 2022 / **Accepted:** 9 May 2022

ABSTRACT

Poly(ethylene oxide) (PEO)-based solid polymer electrolytes (SPEs) are commonly used in lithium metal batteries (LMBs) for their good Li-salt solvating ability and easy processability. However, the relatively low Li-ion conduction ability hinders their further development. In this work, a novel hyperbranched-polyether-type composite solid polymer electrolyte (CSPE) is prepared via a quick cross-linking reaction between aldehyde-terminated polyethylene glycol (PEG) and hyperbranched poly(ethylene imine) (HPEI) in the presence of lithium salt and fluorine-containing Zr-based metal–organic framework (MOF) UiO-66-(F)$_4$. The hydrogen bonds between the fluorine atoms and amino groups in the electrolyte help to the better dispersion of UiO-66-(F)$_4$ in the polymer matrix, which is beneficial to solving the problem of aggregation of nanofillers. Besides, the CSPEs with the functional MOF fillers show improvements in both electrochemical and mechanical properties. Notably, the Li-ion transference number ($t_{\mathrm{Li^+}}$) is considerably enhanced from 0.23 to 0.54. All-solid-state LMBs based on the CSPE also present good cycling performances. A high specific discharge capacity of 141.4 mAh·g^{-1} is remained after 200 cycles at 0.2 C. This study not only provides an effective synthesis method of the cross-linked hyperbranched polymer electrolyte, but also puts forward a new strategy for uniform dispersion of inorganic fillers in CSPEs.

KEYWORDS

hyperbranched cross-linked polymer electrolyte, all-solid-state, metal-organic frameworks, composite, lithium metal batteries

1 Introduction

Lithium-ion batteries (LIBs) are important energy-storage devices that are extensively used in electronic products and electric vehicles. To satisfy the increasing demand for energy storage, countless attempts have been made to enhance both energy density and safety of state-of-the-art LIBs [1–7]. Using solid-state electrolytes (SSEs) is one of the most promising methods because the underlying risk of leakage or even catching fires arising from the commercial liquid organic electrolytes can be avoided [8–10]. In general, SSEs contain two types: inorganic solid electrolytes (ISEs) and solid polymer electrolytes (SPEs) [11, 12]. Compared with ISEs, SPEs are lightweight, soft, stretchable, and easy to process, and have lower interfacial resistance with electrodes, thus have the potential to apply to high-energy-density and flexible devices [13, 14].

Among all the polymer matrices for SPEs, polyether, especially poly(ethylene oxide) (PEO), is the most representative one owing to its comparatively low glass transition temperature (T_g) (−60 °C) and relatively good Li-salt solvating ability [15, 16]. However, due to the high crystallinity of PEO, the Li-ion conduction which mainly takes place in the amorphous phase of the polymer chain is limited [17, 18]. As a result, the ionic conduction of linear PEO-type SPE is as low as 10^{-7} S·cm^{-1} at room temperature [19, 20]. Besides, the strong complexions between the EO segments and Li$^+$ lead to a low lithium ion transference number ($t_{\mathrm{Li^+}}$) (< 0.3) in PEO [21, 22]. A low $t_{\mathrm{Li^+}}$ not only decreases the energy efficiency, but also relates to severer ion concentration polarization in the cell, which is the main cause of lithium dendrite formation [23–25]. Therefore, many efforts have been devoted to solving the above drawbacks of PEO-type SPEs. For example, PEO are copolymerized or blended with polypropylene oxide (PPO) [26], poly(methyl methacrylate) (PMMA) [27], poly(vinylidene fluoride) (PVDF) [28], and polystryene (PS) [29] to increase the proportion of amorphous phase in the polymer matrix. Specially, branched or cross-linked polyethers are used to decrease the crystallinity and reinforce lithium dendrite resistance [30–32]. It is worth noting that nanofillers, such as Al_2O_3 [33], SiO_2 [34], TiO_2 [35], zeolites [36–39], and metal–organic frameworks (MOFs) [40–42], are added to PEO-Li salt complex and show improved electrochemical properties. Among all these nanofillers, MOFs show great advantages due to their porous structures, relatively high Lewis acidity, and structural adjustability. For example, Huo

---

Address correspondence to Wei Liu, weiliu@ucas.edu.cn; Liaoyun Zhang, zhangly@ucas.edu.cn

et al. synthesized a cationic MOF (CMOF) by the nucleophilic substitution of grafted pyridine N based on UiO-66 and applied this CMOF as filler for PEO-type SPE [43]. As a result, the CMOF fillers play an important role in anion adsorption, which leads to a high t_{Li^+} of 0.72 in the composite electrolyte. However, this kind of MOF fillers easily occur the problem of uneven dispersion in the composite blend system. Wang et al. proposed a thiol-branched SPE which prepared by linking the vinyl functionalized UiO-66 and the polyether matrix via C–S–C covalent bonds [44]. This thiol-branched structure offers the SPE surprising ionic conductivity. However, the fabrication of above MOF-polymer composite SPEs (CSPEs) involves complicated modification of the MOF fillers, which is still difficult for practical application. In order to develop new MOF-polymer composite SPEs with easily synthesis and excellent performance, a novel CSPE composed of cross-linked hyperbranched polymer matrix polyethylene glycol (PEG)-hyperbranched poly(ethylene imine) (HPEI), Li-salt lithium bis(trifluoromethane sulfonyl)imide (LiTFSI), and fluorine-containing Zr-based MOF UiO-66-(F)$_4$ is prepared. The PEG-HPEI matrix is synthesized via a facile Schiff's base reaction between aldehyde-terminated PEG and HPEI. In the hyperbranched cross-linked PEG-HPEI electrolyte matrix, the hyperbranched structure can provide more EO units which can conduct Li$^+$ compared with linear PEO matrix, which is beneficial to achieve high ionic conductivity. Moreover, the HPEI segments can provide cross-linking sites, meanwhile the amino groups in HPEI can form hydrogen bonds with fluorine atoms on the MOFs' linkers, which helps to the better dispersion of the MOF fillers and promotes mechanical strength. Importantly, the MOF fillers with nano size, porous structure, and ultra-high Lewis acidity not only can interact with polymer chains and affect their physical or chemical properties, but also immobilize the TFSI$^-$ anions and impurities, which effectively improves the electrochemical properties of the CSPEs. As a result, the as-prepared electrolyte shows higher ionic conductivity after composition (3.01×10^{-5} S·cm^{-1} vs. 7.53×10^{-6} S·cm^{-1} at 30 °C) owing to the decrease of crystallinity of PEG-HPEI caused by addition of the MOF nanofillers. Additionally, the t_{Li^+} is considerably increased from 0.23 to 0.54 due to the strong Lewis acid-base interaction between MOF particles and TFSI$^-$ anions. Consequently, all-solid-state lithium metal batteries (LMBs) assembled with LiFePO$_4$ (LFP) cathodes and the CSPEs also demonstrate good long-cycle performances at 60 °C. A specific discharge capacity of 141.4 mAh·g^{-1} is remained after 200 cycles at 0.2 C. At a higher current rate of 0.5 C, the cell also exhibits a specific discharge capacity of 107.6 mAh·g^{-1} after 100 cycles.

2 Experimental

2.1 Materials and methods

2.1.1 Materials

Zirconyl chloride octahydrate ($ZrOCl_2·8H_2O$, 99.9%, Aladdin), tetrafluoroterephthalic acid (H_2fBDC, 97.0%, Aladdin), terephthalic acid (H_2BDC, 99%, Adamas-beta), acetic acid (99.5%, Macklin), CHO-PEG-CHO (M_W = 4,000 g·mol^{-1}, 95%, 3Achem), and HPEI (M_W = 10,000 g·mol^{-1}, 99%, Aladdin) were used directly after received. LiTFSI (99%, Macklin) was dried at 80 °C under vacuum for 24 h before use. Methanol (99.5%, Beijing Tongguang Fine Chemicals) was dried with 4A molecule sieves before use.

2.1.2 Methods

Synthesis of UiO-66-(F)$_4$ and UiO-66. UiO-66-(F)$_4$ and UiO-66 were synthesized according to a reported work with some modification [45]. In a typical procedure, $ZrOCl_2·8H_2O$ (5.2 mmol) and H_2fBDC (5 mmol) for UiO-66-(F)$_4$ (or H_2BDC (5 mmol) for UiO-66) were suspended in 50 mL of water/acetate acid (3:2 in volume) mixed solvent. The solution was stirred at room temperature for one hour and then heated at 80 °C under reflux for 24 h. The white powder product UiO-66-(F)$_4$ or UiO-66 was collected by centrifugation and washed with methanol for 3 days, during which time the solvent was decanted and fresh methanol was added every 24 h. Finally, the product was dried at 120 °C under vacuum for 24 h.

Preparation of the SPE, CSPE, and PEG-HPEI. For the preparation of SPE or CSPE, the CHO-PEG-CHO and LiTFSI (EO:Li = 15:1, mole ratio) were firstly solvated in methanol and stirred for 20 h. Then appropriate amount of UiO-66-(F)$_4$ was added to the solution and stirred to form a uniform suspension. After that, HPEI (weight ration of HPEI to CHO-PEG-CHO was 1:3) was added into the mixture and stirred at room temperature for 8 h to form the cross-linked network PEG-HPEI. Finally, the reaction mixture was concentrated by rotary evaporation and casted on a PTFE plate. Free-standing electrolyte membranes SPE15-0, CSPE15-9, CSPE15-12, and CSPE15-15 (containing 0 wt.%, 9 wt.%, 12 wt.%, and 15 wt.% UiO-66-(F)$_4$, respectively) were obtained after dried at 50 °C under vacuum for 24 h.

2.2 Characterization

2.2.1 Structural characterization

Fourier transform infrared (FTIR) spectra were recorded on a Bruker Vertex 70 infrared instrument using the attenuated total reflectance (ATR) technique from 4,000 to 400 cm^{-1}. X-ray diffraction (XRD) measurements were implemented on an Automated Multipurpose X-ray Diffractometer Smartlab 9 kW which was operated at 45 kV and 200 mA with a copper target (λ = 1.54 Å, the scanning rate was 10°·min^{-1}). A Hitachi SU8010 field emission scanning electron microscope (SEM) with energy dispersive spectrometry (EDS) was used to acquire the microstructures and morphologies of UiO-66-(F)$_4$, SPE15-0, and CSPE15-12 electrolyte membranes (sputtered with Au for 30 s). The N_2 adsorption–desorption isotherm was acquired by ASAP 2460 (Micrometrics) at 77 K. The specific surface area was calculated based on the Brunauer–Emmett–Teller (BET) equation. The pore size distribution was determined by the density functional theory (DFT) models. Zeta potential of UiO-66-(F)$_4$ particles was tested by a ZETASIZER NANO (Malvern Panalytical) laser particle size/potential analyzer, using deionized water as solvent. Thermal gravimetric analysis (TGA) was obtained on a PerkineElmer TGA 1 series instrument featuring thermal gravimetric analysis at the heating rate of 20 °C·min^{-1} from 30 to 600 °C. Differential scanning calorimetry (DSC) methods were implemented by a Q2000 calorimeter outfitted with TA Instruments running under the protection of nitrogen (the samples were sealed in aluminum pans and the cooling/heating rate was 5 °C·min^{-1}). A tensile testing machine (Instron 5957, the tensile speed was 2 mm·min^{-1}) was used to obtain the stress–strain curve of the SPE15-0 and CSPE15-12.

2.2.2 Electrochemical measurements

The ionic conductivities of electrolyte membranes which were sealed in a stainless-steel (SS) mold were determined by a ModuLab XM electrochemical workstation through electrochemical impedance spectroscopy (EIS) with a method of two-probes. The block electrodes used in the method were SS. The frequency ranged from 1 MHz to 1 Hz, the alternating current (AC) amplitude was 5 mV, and the temperatures ranged from 30 to 80 °C with a step size of 10 °C.

The ionic conductivity was obtained via Eq. (1)

$$\sigma = \frac{L}{SR} \tag{1}$$

where L, S, and R are the thickness of the electrolytes, the contact area of electrodes and electrolytes, and the bulk resistance of the electrolytes, respectively.

The lithium ion transference number (t_{Li^+}) tests of electrolyte membranes were tested in symmetric Li/electrolyte membrane/Li cells at 60 °C. The cells were polarized with a direct current (DC) voltage of 20 mV. AC impedance spectroscopy was tested before and after the polarization (the frequency ranged from 1 MHz to 10 mHz and the oscillation voltage was set as 5 mV).

The t_{Li^+} is evaluated by Eq. (2)

$$t_{\mathrm{Li}^+} = \frac{I_s(\Delta V - I_0R_0)}{I_0(\Delta V - I_sR_s)} \tag{2}$$

where R_0 and I_0 are the initial resistance (the passivating layers of electrolyte membrane and Li metal) and current before polarization, respectively. R_s and I_s are the steady-state resistance and current after polarization, respectively.

The electrochemical windows of electrolyte membranes were obtained on the ModuLab XM electrochemical workstation using fabricated Li/electrolyte membrane/SS coin cells, the linear sweep voltammogram (LSV) was recorded at 60 °C with a scan rate of 3 mV·s^{-1} from 2 to 6 V (vs. Li$^+$/Li).

Galvanostatic cycling of the Li/Li symmetrical cells were conducted at a current density of 0.1 mA·cm^{-2} and a cycle capacity of 0.1 mAh·cm^{-2} (cycled at 60 °C).

The interfacial stability of electrolyte membranes against lithium metal electrodes was obtained by measuring the interfacial resistance of the symmetric Li/electrolyte membrane/Li cells at room temperature (the frequency ranged from 1 MHz to 1 mHz).

Battery performances of the LFP/electrolyte membrane/Li cells were performed using LANHE CT2001A battery testing system at 60 °C with charge–discharge voltage between 2.5 and 4 V. The cathode was composed of LFP (70 wt.%), super P (20 wt.%), and PVDF (10 wt.%).

3 Results and discussion

As illustrated in Fig. 1, the composite hyperbranched polymer electrolyte consists of polymer matrix PEG-HPEI, Li salt LiTFSI, and nanofillers UiO-66-(F)$_4$. The cross-linked hyperbranched copolymer PEG-HPEI is synthesized via the quick Schiff's base reaction between CHO-PEG-CHO and HPEI. The EO units in PEG segments can serve as Li$^+$ conductor. While the amino groups in HPEI segments on the one hand provide cross-linking sites, on the other hand form hydrogen bonds with the fluorine atoms of UiO-66-(F)$_4$, which helps to the better dispersion of the MOF fillers in the polymer matrix. As shown in Fig. S1 in the Electronic Supplementary Material (ESM), no obvious precipitation can be observed after resting the precursor suspension of CSPE15-12 for 12 h. Besides, the incorporated UiO-66-(F)$_4$ nanoparticles with abundant unsaturated Zr sites can immobilize the TFSI$^-$ anions via the Lewis acid-base interaction and thus facilitate the lithium ion transport in the polymer electrolyte.

The crystal structure of as-synthesized UiO-66-(F)$_4$ was confirmed by XRD (Fig. S2 in the ESM), the characteristic peaks of UiO-66-(F)$_4$ fit well with the simulated pattern of UiO-66. Figure S3(a) in the ESM shows the FTIR spectrum of the as-synthesized UiO-66-(F)$_4$. The asymmetrical and symmetrical stretching vibration of carbonyl in fBDC linkers locate at 1,619 and 1,404 cm^{-1}, respectively [46, 47]. The adsorption band at 654 cm^{-1} is ascribed to the metal cluster Zr-μ_3-O [46]. Furthermore, the characteristic adsorption bands of μ_3-OH linked with Zr atoms in both UiO-66-(F)$_4$ and UiO-66 are compared in the high frequency region of FTIR spectra (Fig. S3(b) in the ESM). The adsorption bands of Zr$_3$(μ_3-OH) in UiO-66-(F)$_4$ and UiO-66 appear at 3,615 and 3,672 cm^{-1}, respectively, which suggests a stronger acidity of the μ_3-OH in UiO-66-(F)$_4$ due to the electron-deficient property of fBDC linkers [47]. The higher Lewis acidity of UiO-66-(F)$_4$ fillers is critical for the enhancement of ionic conductivity and t_{Li^+}. Additionally, the N$_2$ adsorption–desorption isotherm test is used for determining the porous structure of UiO-66-(F)$_4$. The result shows that the specific surface area of UiO-66-(F)$_4$ particles is as high as 653.9612 m^2·g^{-1} (Fig. S4(a) in the ESM) and pore diameters are less than 1 nm (Fig. S4(b) in the ESM).

The structures of the as-prepared polymer matrix PEG-HPEI and electrolyte membranes were also confirmed by FTIR spectra. As shown in Fig. 2, the adsorption bands of –NH$_2$, –C–O–C–, and –C=N– locate at 3,400–3,100, 1,096, and 1,634 cm^{-1} in the spectrum of PEG-HPEI, respectively. The adsorption band of –C=O of aldehyde group in the spectrum of CHO-PEG-CHO at 1,731 cm^{-1} (Fig. S5 in the ESM) cannot be seen in the as-

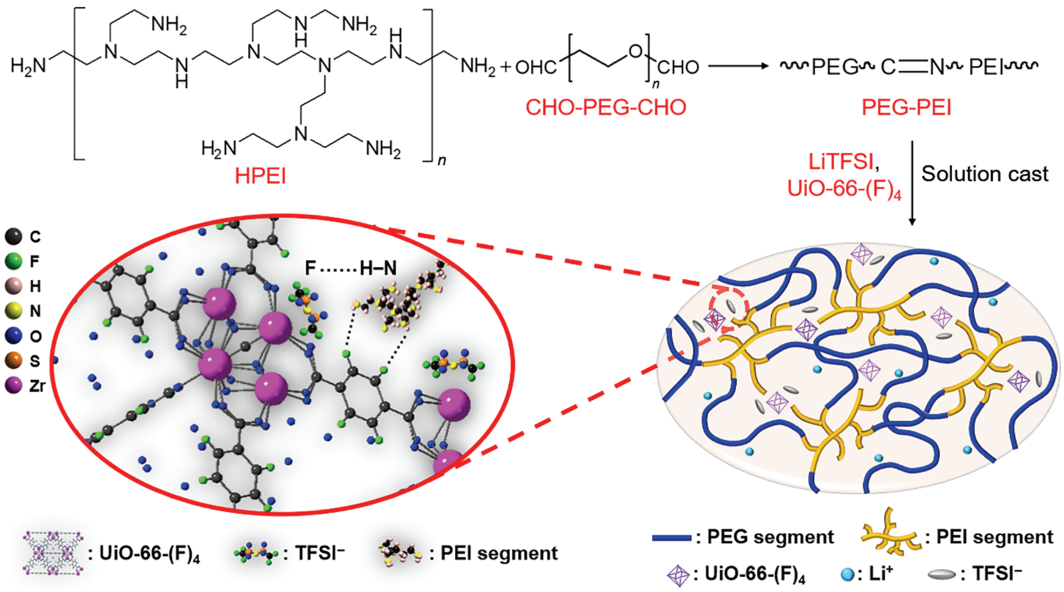

Figure 1 Structure and schematic Li-ion transport model of UiO-66-(F)$_4$ composite solid cross-linked polymer electrolyte.

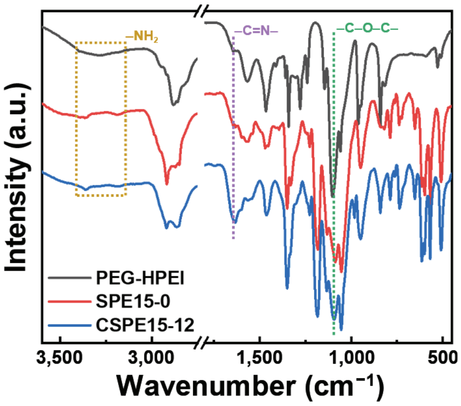

Figure 2 FTIR spectra of PEG-HPEI, SPE15-0, and CSPE15-12.

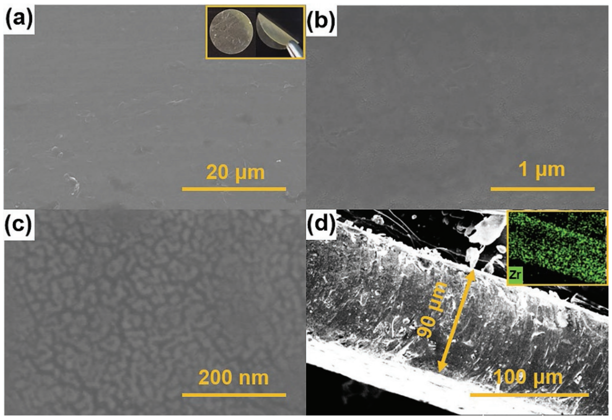

Figure 3 (a)–(c) Surface SEM images and (d) side-view SEM image of CSPE15-12 (insets of (a) are digital pictures of CSPE15-12 membranes at flat and bended states; inset of (d) is the corresponding Zr element EDS mapping image).

synthesized PEG-HPEI, while the adsorption band of –C=N is observed, implying successful Schiff's base reaction between CHO-PEG-CHO and HPEI. And it is worth mentioning that the adsorption band at around 1,634 cm^{-1} in the spectrum of CSPE15-12 is stronger and wider than that of CSPE15-0, which may be attributed to common contribution of vibration adsorption of –C=N– and –C=O of –COO in fBDC linkers.

SEM was applied to characterize the morphologies of the MOF fillers and electrolyte membranes. As presented in Figs. S6(a) and S6(b) in the ESM, the particle size of UiO-66-(F)$_4$ is around 400 nm, which helps the fillers to penetrate into the polymer matrix. Figures S7(a)–S7(c) in the ESM and Figs. 3(a)–3(c) show the surface SEM images of SPE15-0 and CSPE15-12, respectively. The electrolyte membranes are flat in micro-level, which contributes to achieve good interfacial contact with electrodes. Furthermore, the CSPE15-12 membrane is self-standing and flexible (inset in Fig. 3(a)), and thus has the potential to be used in flexible devices. Moreover, the cross-linked structure of the polymer matrix can be clearly seen in Fig. S7(c) in the ESM and Fig. 3(c), which is conducive to providing ion transport path. The side-view SEM and corresponding EDS mapping images of CSPE15-12 are shown in Fig. 3(d). The thickness of CSPE15-12 is around 90 μm. And the EDS mapping image of Zr element suggests that the MOF fillers can distribute uniformly in the composite electrolyte.

High thermal stability and mechanical strength are critical for SPEs with high safety. Figure 4(a) shows the TGA curves of SPE15-0 and CSPE15-12. Both SPE15-0 and CSPE15-12 maintain steady up to 340 °C, which proves a good thermal stability of the electrolytes and thus can guarantee the wide-temperature range safety of the cells. As exhibited in the tensile stress–strain curves in Fig. 4(b), the tensile stress of CSPE15-12 is 1.477 MPa, while the value of SPE15-0 is only 0.211 MPa. What is more, the elongation at break is elevated from 28% to 58% after composition. These results indicate that the UiO-66-(F)$_4$ fillers can not only enhance the rigidity of the membranes, but also improve the extensibility, which may result from the existence of the hydrogen bond between the fillers and polymer chains. To demonstrate the existence of hydrogen-bond interactions between the fillers and polymer chains, we conducted the related tests of FTIR and ^{1}H nuclear magnetic resonance (NMR). As shown in Fig. S8(a) in the ESM, the ^{1}H NMR was employed to study the hydrogen-bonds interactions between CHO-PEG-CHO, HPEI, and the MOF fillers. A characteristic peak locating at around 3.60–3.65 ppm is attributable to ether–oxygen bond (–CH$_2$–CH$_2$–O–) of CHO-PEG-CHO. The ^{1}H NMR signal of HPEI-PEG after Schiff base reaction shows an upshifting of about 9.6 × 10^{-4} ppm, which is assigned to the hydrogen-bonds interactions between –NH$_2$– from HPEI and –CH$_2$–CH$_2$–O– from CHO-PEG-CHO. In contrast, the relatively stronger chemical shift variation for HPEI-PEG-MOF can be observed in the ^{1}H NMR after introducing the UiO-66-(F)$_4$ fillers into the polymer matrix. This result verified the existence of the hydrogen-bond interactions between the fillers and polymer chains. Furthermore, Fig. S8(b) in the ESM presents the FTIR spectra of CHO-PEG-CHO, HPEI-PEG, and HPEI-PEG-MOF in the range from 1,250–750 cm^{-1}. The characteristic adsorption peaks at 1,057 and 1,021 cm^{-1} can be clearly observed in pure CHO-PEG-CHO, which are related to the vibration of the ether–oxygen bond (C–O–C). Compared to the pure CHO-PEG-CHO, the C–O–C stretching-resulted peak positions of HPEI-PEG-MOF shifted from 1,057 to 1,059 cm^{-1} and from 1,021 to 1,040 cm^{-1}, while the shape of the absorbance peaks of ether–oxygen bond also changed. These results also indicated the hydrogen-bond interactions between the fillers and polymer chains.

For electrochemical study, the Li salt content in CSPEs was set to a fixed mole ratio of EO:Li = 15:1. To achieve high ionic

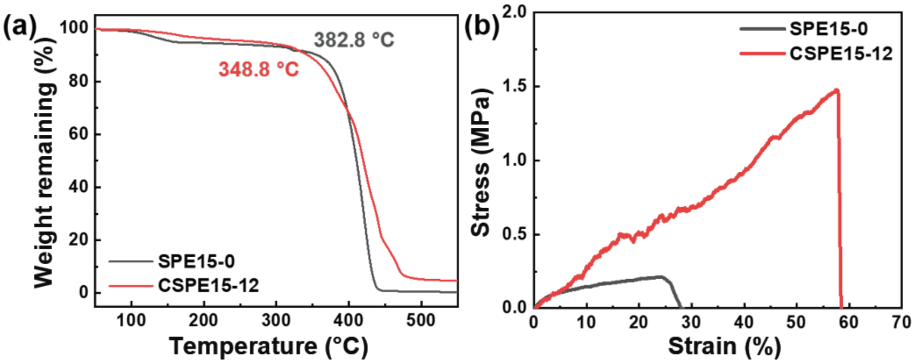

Figure 4 (a) TGA curves of SPE15-0 and CSPE15-12. (b) Stress–strain curves of SPE15-0 and CSPE15-12 membranes.

conductivity, the content of UiO-66-(F)$_4$ was optimized. As shown in Fig. 5(a), the ionic conductivities of the prepared electrolytes increase with the increase of the temperature. This is due to the conduction of lithium-ions in the electrolytes mainly depends on the polymer chains movement and the interactions between the Li^+ and –CH_2–CH_2–O– segments. When the temperature rises, the mobility of polymer segments and dissociation of lithium salt are both promoted. Consequently, the ionic conductivities of the prepared electrolytes increase with the increase of the temperature. Besides, the ionic conductivities of the electrolyte membranes first increase with the increase of content of the UiO-66-(F)$_4$ and then decrease. A lower ionic conductivity of CSPE15-15 may be caused by the aggregation of excessive nanofillers. The highest ionic conductivity (3.01×10^{-5} S·cm^{-1} at 30 °C, the corresponding EIS see Fig. S9 in the ESM) is obtained when 12 wt.% UiO-66-(F)$_4$ is added. Therefore, the CSPE15-12 membranes are chosen to conduct the following tests. By contrast, the ionic conductivity of SPE15-0 was only 7.53×10^{-6} S·cm^{-1} at 30 °C. The enhancement of ionic conductivity after composition can be mainly attributed to the following two reasons. First, it is well-known that the polyether-based SPEs often suffer from low Li^+ conductivities due to high crystallinity of the polymer matrix. However, the nanofillers, with large specific surface area and porous structure (Figs. S4(a) and S4(b) in the ESM), can decrease the crystallinity of the polymer matrix by destructing its ordered arrangement, which is beneficial to a fast Li-ion conduction in amorphous area. In addition, the interaction between Zr open sites and $TFSI^-$ anions promotes the dissociation of Li salt, which leads to a higher free ion content. The former reason can be verified by XRD and DSC characterization. As presented in Fig. 5(b), for CSPE15-12, the two characteristic peaks ascribed to the PEG-HPEI polymer at 18.8° and 23.1° are reduced significantly compared with those of SPE15-0. The result suggests that the nano-sized MOF fillers can reduce the crystallinity of the polymer. DSC tests were also used to study the effect of MOF fillers on the crystallinity of PEG-HPEI (Fig. 5(c)). Apparently, the melting enthalpy of CSPE15-12 (34.92 J·g^{-1}) was much less than SPE15-0 (54.72 J·g^{-1}), indicating the important role of UiO-66-(F)$_4$ fillers in decreasing the crystallinity of the polymer matrix. These results are in accordance with the XRD results. The latter reason can be verified by the FTIR and Raman results. Figure 5(d) shows the magnified FTIR spectra of the electrolyte membranes in the range of 1,400–1,150 cm^{-1}. The two strongest adsorption bands at 1,350 and 1,183 cm^{-1} are ascribed to the asymmetrical stretching vibration of –SO_2 and –CF_3 groups in free $TFSI^-$ anions. While those low-intensity shoulder bands between these two bands belong to ion pairs (Li^+TFSI^-). For CSPE15-12, the shoulder bands of –SO_2 and –CF_3 groups in ion pairs locate at 1,333 and 1,227 cm^{-1}, respectively. But for SPE15-0, the stretching vibration band of –SO_2 groups in ion pairs at 1,330 cm^{-1} presents a lower-wavenumber shift, meanwhile an additional adsorption band of –CF_3 group in ion pairs appears at 1,250 cm^{-1} [48]. Importantly, the relative intensity of the band at 1,350 cm^{-1} belonging to the absorption of $TFSI^-$ free ion increased after the addition of UiO-66-(F)$_4$. And as shown in Fig. S10 in the ESM, the Raman signals consist of two peaks located at 740 and around 743 cm^{-1}, which are assigned to the dissociated ions and ion pairs. In contrast, the content of the dissociated ions increases from 69% for SPE15-0 to 84% for CSPE15-12, suggesting that the introduction of UiO-66-(F)$_4$ fillers is surely conducive to the dissociation of LiTFSI. Therefore, these results imply that there are more free ions in CSPE15-12, which indicates the UiO-66-(F)$_4$ fillers with strong Lewis acidity do play an important role in restraining the $TFSI^-$ anions and thus help to the dissociation of LiTFSI.

The lithium-ion transference number (t_{Li^+}) value is another critical factor for electrolytes. As presented in Figs. 6(a) and 6(b), the t_{Li^+} value of the obtained electrolyte is improved from 0.23 to 0.54 after composition. The reason for the significant enhancement of t_{Li^+} was further explored by a zeta potential analysis, the result is shown in Fig. S11 in the ESM. The zeta potential of UiO-66-(F)$_4$ fillers dispersed in water is 24.9 mV. So, it is obvious that the MOF fillers possess positive surface charge center in the CSPE and thus immobilize the $TFSI^-$ anions, which contributes to an efficient Li-ion migration.

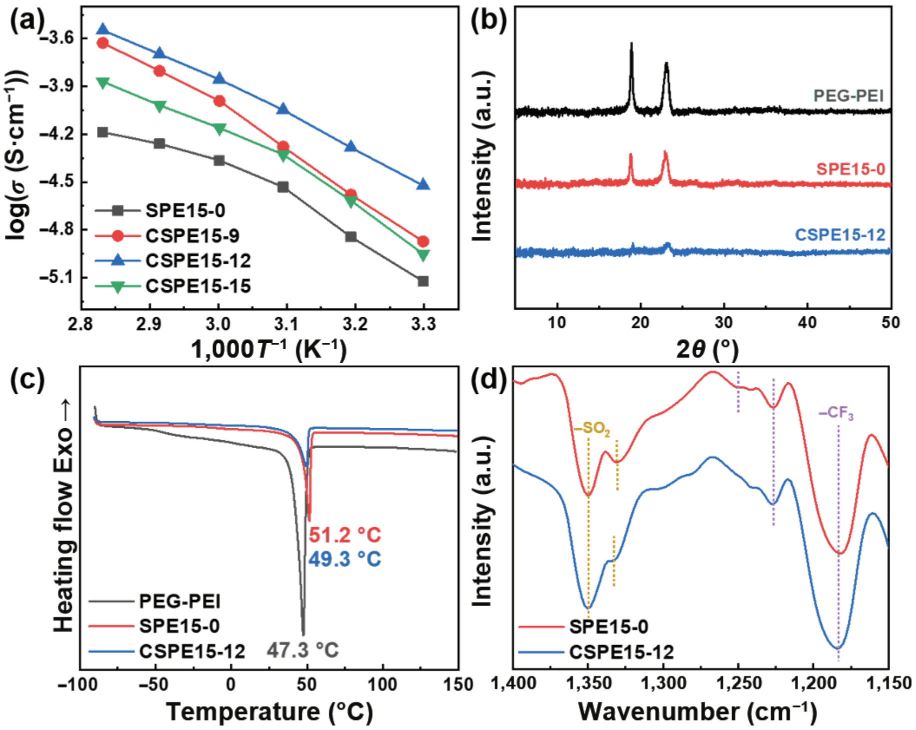

Figure 5 (a) Ionic conductivities of SPE and CSPEs at different temperatures. (b) XRD patterns of PEG-PEI, SPE15-0, and CSPE15-12. (c) DSC curves of PEG-PEI, SPE15-0, and CSPE15-12. (d) FTIR spectra of SPE15-0 and CSPE15-12 in the range from 1,400 to 1,150 cm^{-1}.

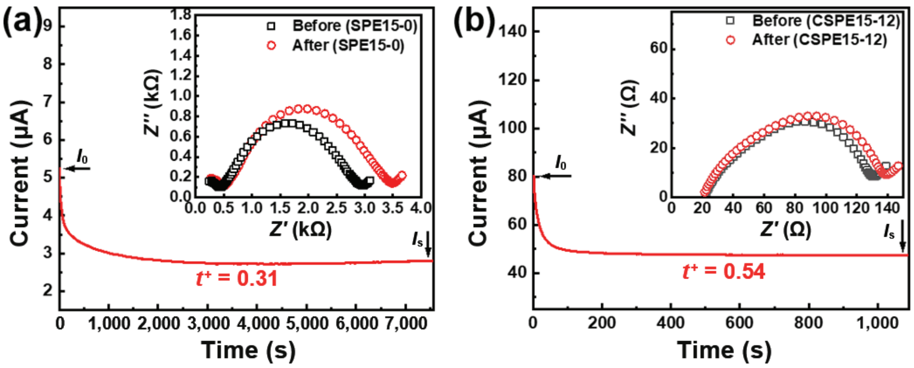

Figure 6 DC polarization curves of (a) Li/SPE15-0/Li and (b) Li/CSPE15-12/Li cells (insets are AC impedance spectra of the symmetric cells before and after polarization).

Electrochemical stability of the electrolyte membranes is evaluated by LSV using asymmetrical cells. As shown in Fig. 7, after the addition of the MOF fillers, the electrochemical window of the electrolyte becomes broaden from 4.0 to 4.3 V. Compared to SPE15-0, the complexation between UiO-66-(F)$_4$'s Zr sites and the EO segments may change the chemical environment of the polymer chains, thus delays the oxidation of EO segments [49]. On the other side, the pore size distribution of UiO-66-(F)$_4$ fillers centered at 0.64 and 1.25 nm. The nano-sized pores of the fillers can immobilize some moisture in the electrolyte (such as H_2O and CH_3OH), which is beneficial to promoting the electrochemical stability (Fig. S4(b) in the ESM).

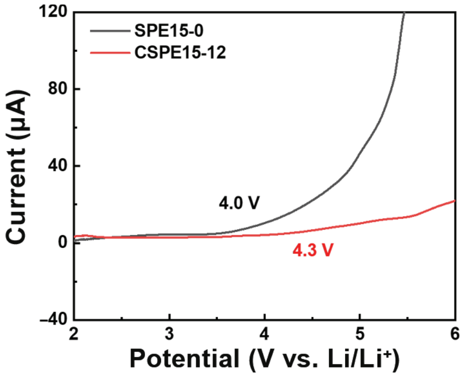

Figure 7 LSV of Li/SPE15-0/SS and Li/CSPE15-12/SS cells.

The interfacial compatibilities of the electrolyte membranes against Li anodes are studied by EIS of the Li/electrolyte membrane/Li cells after different aging times at room temperature. As can be seen in Figs. 8(a) and 8(b), the interfacial resistance of the electrolyte membranes can be approximately obtained from the diameter of the semicircle in the medium frequency range. It is obvious that the interfacial resistance of CSPE15-12 is much smaller and steadier than that of SPE15-0 during the 14 days. This may be because the UiO-66-(F)$_4$ fillers with porous structure can provide faster and continuous Li-ion transport path for the composite electrolyte. Furthermore, the MOF particles with high porosity can adsorb some impurities, which contributes to the long-range stability of the electrolyte/Li interface. Additionally, the Li plating/stripping tests were conducted at 60 °C and a current density of 0.1 mA·cm^{-2} (Fig. 8(c)). Both the symmetric cells assembled with SPE15-0 and CSPE15-12 show a lower overpotential of around 80 mV. Although the Li/SPE15-0/Li cell show a little smaller polarization, for the softer contact between the pure polymer and Li foils, the

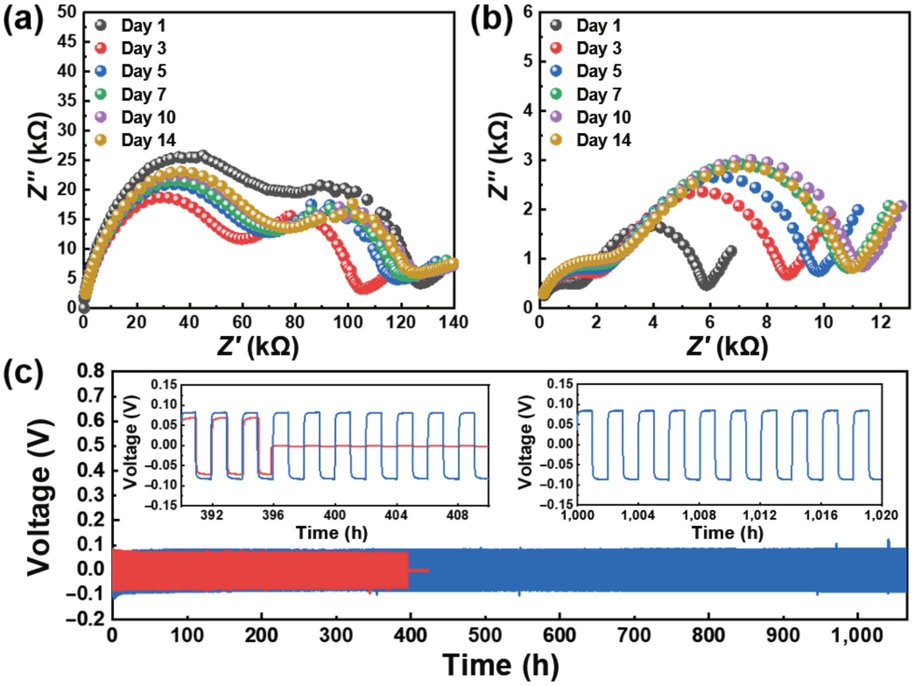

Figure 8 Impedance profiles of (a) Li/SPE15-0/Li and (b) Li/CSPE15-12/Li symmetric cells after different aging times at room temperature. (c) Li plating/stripping curves of Li/SPE15-0/Li and Li/CSPE15-12/Li symmetric cells at a current density of 0.1 mA·cm^{-2} and a cycle capacity of 0.1 mAh·cm^{-2} (insets are Li plating/stripping curves at the selected period).

Li/SPE15-0/Li cell encountered short-cut after cycled for only 396 h. In contrast, the Li/CSPE15-12/Li cell stably cycled for more than 1,000 h under the same condition, which contributed to the porous structure of MOF provided faster and continuous Li-ion transport path for the composite electrolyte, realizing the high Li-ion transference number. And the high Li-ion transference number ensures efficient Li-ion migration, which significantly suppressed concentration polarization and lithium dendrite formation. More importantly, the fluorine element doped in UiO-66-(F)$_4$ is conducive to forming a stable interfacial layer during cell cycling. This result suggests the as-obtained CSPE has the potential to inhibit the pierce of lithium dendrites.

CR2025 coin cells were assembled with LFP cathodes, electrolyte membranes (CSPE15-12 or SPE15-0), and Li anodes. Figure 9(a) shows the long-cycle performances of the all-solid-state cells at a current rate of 0.2 C. The LFP/CSPE15-12/Li cell remained a high capacity of 141.4 mAh·g^{-1} after 200 cycles. However, the cell based on SPE15-0 fails after only 26 cycles. As can be seen in the corresponding voltage–capacity curves (Figs. S12(a) and S12(b) in the ESM), the polarization of LFP/CSPE15-12/Li after 200 cycles is even much less than that of LFP/SPE15-0/Li after 20 cycles, which is mainly due to the more efficient Li$^+$ transfer and higher interfacial stability between CSPE15-12 and the cathode. When charged/discharged at a higher current rate of 0.5 C, the LFP/CSPE15-12/Li cell delivers a specific capacity of 107.6 mAh·g^{-1} after 100 cycles (Fig. 9(b), corresponding charge–discharge curves see Fig. S13 in the ESM), which suggests the all-solid-state cell possesses a fast charging/discharging ability. Rate performances of the LFP/CSPE15-12/Li cell were also tested and the results are shown in Fig. 9(c) (corresponding charge–discharge curves see Fig. S14 in the ESM). Specific capacities of 136.9, 134.3, 125.8, 116.5, and 72.9 mAh·g^{-1} are obtained at current densities of 0.1, 0.2, 0.3, 0.5, and 1 C, respectively. Besides, when the rate turns back to 0.1 C, the capacity recovers to 139.4 mAh·g^{-1}. Figure 9(d) presents the CV curves of the LFP/CSPE15-12/Li cell. The oxidation and reduction peaks of the Fe^{3+}/Fe^{2+} redox couple locate at 3.7 and 3.2 V, respectively. And it can be found that the peak intensity increases along with the cycle numbers, which indicates that the cell can be activated during the cycling, thus the interfacial contact is improved and the materials utilization is also increased. Additionally, the shape and position of the peaks remain stable in the first 3 cycles, which proves the CSPE15-12 membrane exhibits good redox reversibility against the LFP cathodes.

The good cycling performances suggest that the LFP/CSPE15-12/Li all-solid-state batteries have the potential to be applied in high-energy-density or even flexible devices. As shown in Fig. 9(e), the assembled all-solid-state coin cells can power 3 light emitting dioxide (LED) bulbs in parallel with different colors. Furthermore, pouch cell assembled with the same electrolyte and electrode materials can power a LED bulb at flat, folded, needle-pierced, and cut states (Figs. 9(f)–9(i)).

4 Conclusions

In this work, a novel composite all-solid-state polymer electrolyte containing MOF fillers UiO-66-(F)$_4$ and hyperbranched polyether-based polymer matrix is prepared. Thanks to the hydrogen bond interaction between the nanofillers and the PEG-HPEI matrix, the dispersibility of the MOF particles in the hybrid system can be effectively improved, thus our newly-prepared CSPE possesses good electrochemical, thermal, and mechanical properties as well as a high filler load of 12 wt.%. The electrolyte with MOF fillers exhibits an ionic conductivity of 3.01 × 10^{-5} S·cm^{-1} at 30 °C and a high t^+ of 0.54. These values are much higher than those of the electrolyte without MOF fillers, indicating a more effective Li$^+$ conduction after composition of the MOF fillers. Besides, the CSPE also shows broader electrochemical window, better compatibility with Li anodes, good thermal stability, and excellent mechanical properties. Moreover, the fabricated all-solid-state Li metal batteries based on the electrolyte with MOF fillers present better cycle performances. Concretely, the LFP/CSPE15-12/Li cell maintains stable and delivered a specific capacity of 141.4 mAh·g^{-1} after 200 cycles, while the LFP/SPE15-0/Li cell without MOF fillers

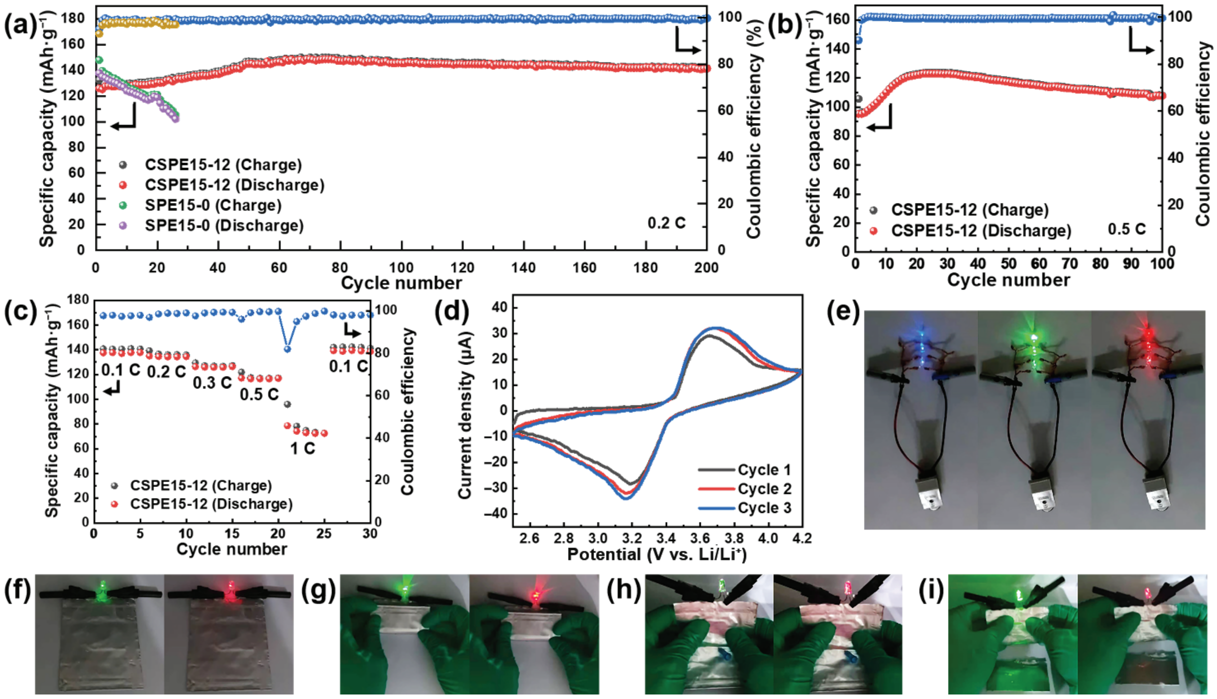

Figure 9 Long cycle performances at 60 °C of (a) LFP/CSPE15-12/Li (solid balls) and LFP/SPE15-0/Li (hollow balls) all-solid state coin cells at 0.2 C and (b) LFP/CSPE15-12/Li at 0.5 C. (c) Rate performance of LFP/SPE15-12/Li. (d) Cyclic voltammetry curves of the LFP/CSPE15-12/Li cell at a scan rate of 0.1 mV·s^{-1}. Images of (e) the LFP/CSPE15-12/Li cell powering 3 LED bulbs in parallel and the LFP/CSPE15-12/Li pouch cell powering a LED bulb at (f) flat, (g) folded, (h) needle-pierced, and (i) cut states.

fails at the 26th cycle with a lower capacity. At a higher current rate of 0.5 C, the LFP/CSPE15-12/Li cell shows a capacity of 107.6 mAh·g^{-1} and a Coulombic efficiency close to 100% after 100 cycles. Specific capacities of 136.9, 134.3, 125.8, 116.5, and 72.9 mAh·g^{-1} are obtained when the LFP/CSPE15-12/Li cell is cycled at 0.1, 0.2, 0.3, 0.5, and 1 C, respectively. In addition, the coin and pouch cell based on CSPE15-12 can power LED bulbs with different colors. This work not only can provide some new strategies for the synthesis of the cross-linked polymer electrolyte and the dispersion of the fillers, but also exhibits a great potential application of this type of all-solid-state MOF composite hyperbranched polymer electrolyte in the high-energy-density solid lithium batteries.

Acknowledgements

This work was supported by the National Natural Science Foundation of China (Nos. 52073285 and 11975238) and the authors also express gratitude for the help from the analysis and testing center at the University of Chinese Academy of Sciences.

Electronic Supplementary Material: Supplementary material (further details of the preparation procedures of UiO-66-(F)$_4$ and the CSPEs, characterization of the electrolyte materials, and electrochemical measurements) is available in the online version of this article at https://doi.org/10.1007/s12274-022-4523-z.

References

[1] Li, N. W.; Yin, Y. X.; Yang, C. P.; Guo, Y. G. An artificial solid electrolyte interphase layer for stable lithium metal anodes. *Adv. Mater.* **2016**, *28*, 1853–1858.

[2] Zhao, J.; Lu, Z. D.; Wang, H. T.; Liu, W.; Lee, H. W.; Yan, K.; Zhuo, D.; Lin, D. C.; Liu, N.; Cui, Y. Artificial solid electrolyte interphase-protected Li$_x$Si nanoparticles: An efficient and stable prelithiation reagent for lithium-ion batteries. *J. Am. Chem. Soc.* **2015**, *137*, 8372–8375.

[3] Wang, Z. C.; Sun, Y. Y.; Mao, Y. Y.; Zhang, F. R.; Zheng, L.; Fu, D. S.; Shen, Y. B.; Hu, J. C.; Dong, H. L.; Xu, J. J. et al. Highly concentrated dual-anion electrolyte for non-flammable high-voltage Li-metal batteries. *Energy Stor. Mater.* **2020**, *30*, 228–237.

[4] Yu, L.; Chen, S. R.; Lee, H.; Zhang, L. C.; Engelhard, M. H.; Li, Q. Y.; Jiao, S. H.; Liu, J.; Xu, W.; Zhang, J. G. A localized high-concentration electrolyte with optimized solvents and lithium difluoro(oxalate)borate additive for stable lithium metal batteries. *ACS Energy Lett.* **2018**, *3*, 2059–2067.

[5] Liu, Y. M.; Qin, X. Y.; Zhou, D.; Xia, H. Y.; Zhang, S. Q.; Chen, G. H.; Kang, F. Y.; Li, B. H. A biscuit-like separator enabling high performance lithium batteries by continuous and protected releasing of NO$_3^-$ in carbonate electrolyte. *Energy Stor. Mater.* **2020**, *24*, 229–236.

[6] Sun, C. W.; Liu, J.; Gong, Y. D.; Wilkinson, D. P.; Zhang, J. J. Recent advances in all-solid-state rechargeable lithium batteries. *Nano Energy* **2017**, *33*, 363–386.

[7] Yan, W. Q.; Gao, X. W.; Jin, X.; Liang, S. S.; Xiong, X. S.; Liu, Z. C.; Wang, Z. G.; Chen, Y. H.; Fu, L. J.; Zhang, Y. et al. Nonporous gel electrolytes enable long cycling at high current density for lithium-metal anodes. *ACS Appl. Mater. Interfaces* **2021**, *13*, 14258–14266.

[8] Liu, B. H.; Jia, Y. K.; Yuan, C. H.; Wang, L. B.; Gao, X.; Yin, S.; Xu, J. Safety issues and mechanisms of lithium-ion battery cell upon mechanical abusive loading: A review. *Energy Stor. Mater.* **2020**, *24*, 85–112.

[9] Perea, A.; Dontigny, M.; Zaghib, K. Safety of solid-state Li metal battery: Solid polymer versus liquid electrolyte. *J. Power Sources* **2017**, *359*, 182–185.

[10] Castillo, J.; Qiao, L. X.; Santiago, A.; Judez, X.; De Buruaga, A. S.; Jiménez-Martín, G.; Armand, M.; Zhang, H.; Li, C. M. Perspective of polymer-based solid-state Li-S batteries. *Energy Mater.* **2022**, *2*, 200003.

[11] Janek, J.; Zeier, W. G. A solid future for battery development. *Nat. Energy* **2016**, *1*, 16141.

[12] Fan, L.; Wei, S. Y.; Li, S. Y.; Li, Q.; Lu, Y. Y. Recent progress of the solid-state electrolytes for high-energy metal-based batteries. *Adv. Energy Mater.* **2018**, *8*, 1702657.

[13] Zhang, Q. Q.; Liu, K.; Ding, F.; Liu, X. J. Recent advances in solid polymer electrolytes for lithium batteries. *Nano Res.* **2017**, *10*, 4139–4174.

[14] Wan, J. Y.; Xie, J.; Kong, X.; Liu, Z.; Liu, K.; Shi, F. F.; Pei, A.; Chen, H.; Chen, W.; Chen, J. et al. Ultrathin, flexible, solid polymer composite electrolyte enabled with aligned nanoporous host for lithium batteries. *Nat. Nanotechnol.* **2019**, *14*, 705–711.

[15] Mindemark, J.; Lacey, M. J.; Bowden, T.; Brandell, D. Beyond PEO—Alternative host materials for Li$^+$-conducting solid polymer electrolytes. *Prog. Polym. Sci.* **2018**, *81*, 114–143.

[16] Zhang, Y. H.; Lu, W.; Cong, L. N.; Liu, J.; Sun, L. Q.; Mauger, A.; Julien, C. M.; Xie, H. M.; Liu, J. Cross-linking network based on poly(ethylene oxide): Solid polymer electrolyte for room temperature lithium battery. *J. Power Sources* **2019**, *420*, 63–72.

[17] Waletzko, R. S.; Korley, L. T. J.; Pate, B. D.; Thomas, E. L.; Hammond, P. T. Role of increased crystallinity in deformation-induced structure of segmented thermoplastic polyurethane elastomers with PEO and PEO-PPO-PEO soft segments and HDI hard segments. *Macromolecules* **2009**, *42*, 2041–2053.

[18] Xi, J. Y.; Qiu, X. P.; Zheng, S. X.; Tang, X. Z. Nanocomposite polymer electrolyte comprising PEO/LiClO$_4$ and solid super acid: Effect of sulphated-zirconia on the crystallization kinetics of PEO. *Polymer* **2005**, *46*, 5702–5706.

[19] Idris, N. H.; Senin, H. B.; Arof, A. K. Dielectric spectra of LiTFSI-doped chitosan/PEO blends. *Ionics* **2007**, *13*, 213–217.

[20] Yan, X. J.; Peng, B.; Hu, B. W.; Chen, Q. PEO-urea-LiTFSI ternary complex as solid polymer electrolytes. *Polymer* **2016**, *99*, 44–48.

[21] Gorecki, W.; Jeannin, M.; Belorizky, E.; Roux, C.; Armand, M. Physical properties of solid polymer electrolyte PEO(LiTFSI) complexes. *J. Phys.:Condens. Matter* **1995**, *7*, 6823–6832.

[22] Xiao, Z. L.; Zhou, B. H.; Wang, J. R.; Zuo, C.; He, D.; Xie, X. L.; Xue, Z. G. PEO-based electrolytes blended with star polymers with precisely imprinted polymeric pseudo-crown ether cavities for alkali metal ion batteries. *J. Membr. Sci.* **2019**, *576*, 182–189.

[23] Lu, Y. Y.; Tikekar, M.; Mohanty, R.; Hendrickson, K.; Ma, L.; Archer, L. A. Stable cycling of lithium metal batteries using high transference number electrolytes. *Adv. Energy Mater.* **2015**, *5*, 1402073.

[24] Deng, K. R.; Qin, J. X.; Wang, S. J.; Ren, S.; Han, D. M.; Xiao, M.; Meng, Y. Z. Effective suppression of lithium dendrite growth using a flexible single-ion conducting polymer electrolyte. *Small* **2018**, *14*, 1801420.

[25] Chen, L.; Fan, L. Z. Dendrite-free Li metal deposition in all-solid-state lithium sulfur batteries with polymer-in-salt polysiloxane electrolyte. *Energy Stor. Mater.* **2018**, *15*, 37–45.

[26] Xue, R. J.; Angell, C. A. High ionic conductivity in PEO. PPO block polymer + salt solutions. *Solid State Ion.* **1987**, *25*, 223–230.

[27] Ghelichi, M.; Qazvini, N. T.; Jafari, S. H.; Khonakdar, H. A.; Farajollahi, Y.; Scheffler, C. Conformational, thermal, and ionic conductivity behavior of PEO in PEO/PMMA miscible blend: Investigating the effect of lithium salt. *J. Appl. Polym. Sci.* **2013**, *129*, 1868–1874.

[28] Cui, Z. Y.; Xu, Y. Y.; Zhu, L. P.; Wang, J. Y.; Xi, Z. Y.; Zhu, B. K. Preparation of PVDF/PEO-PPO-PEO blend microporous membranes for lithium ion batteries via thermally induced phase separation process. *J. Membr. Sci.* **2008**, *325*, 957–963.

[29] Young, W. S.; Albert, J. N. L.; Schantz, A. B.; Epps, T. H. Mixed-salt effects on the ionic conductivity of lithium-doped PEO-containing block copolymers. *Macromolecules* **2011**, *44*, 8116–8123.

[30] Marzantowicz, M.; Dygas, J. R.; Krok, F.; Tomaszewska, A.; Florjańczyk, Z.; Zygadło-Monikowska, E.; Lapienis, G. Star-branched poly(ethylene oxide) LiN(CF$_3$SO$_2$)$_2$: A promising polymer electrolyte. *J. Power Sources* **2009**, *194*, 51–57.

[31] Zheng, Y. W.; Li, X. W.; Li, C. Y. A novel de-coupling solid

polymer electrolyte via semi-interpenetrating network for lithium metal battery. *Energy Stor. Mater.* **2020**, *29*, 42–51.

[32] Khurana, R.; Schaefer, J. L.; Archer, L. A.; Coates, G. W. Suppression of lithium dendrite growth using cross-linked polyethylene/poly(ethylene oxide) electrolytes: A new approach for practical lithium-metal polymer batteries. *J. Am. Chem. Soc.* **2014**, *136*, 7395–7402.

[33] Jayathilaka, P. A. R. D.; Dissanayake, M. A. K. L.; Albinsson, I.; Mellander, B. E. Effect of nano-porous Al_2O_3 on thermal, dielectric and transport properties of the $(PEO)_9$LiTFSI polymer electrolyte system. *Electrochim. Acta* **2002**, *47*, 3257–3268.

[34] Lin, D. C.; Liu, W.; Liu, Y. Y.; Lee, H. R.; Hsu, P. C.; Liu, K.; Cui, Y. High ionic conductivity of composite solid polymer electrolyte via *in situ* synthesis of monodispersed SiO_2 nanospheres in poly(ethylene oxide). *Nano Lett.* **2016**, *16*, 459–465.

[35] Lin, C. W.; Hung, C. L.; Venkateswarlu, M.; Hwang, B. J. Influence of TiO_2 nano-particles on the transport properties of composite polymer electrolyte for lithium-ion batteries. *J. Power Sources* **2005**, *146*, 397–401.

[36] Munichandraiah, N.; Scanlon, L. G.; Marsh, R. A.; Kumar, B.; Sircar, A. K. Influence of zeolite on electrochemical and physicochemical properties of polyethylene oxide solid electrolyte. *J. Appl. Electrochem.* **1995**, *25*, 857–863.

[37] Li, W. W.; Zhang, S. P.; Wang, B. R.; Gu, S.; Xu, D.; Wang, J. N.; Chen, C. H.; Wen, Z. Y. Nanoporous adsorption effect on alteration of the Li^+ diffusion pathway by a highly ordered porous electrolyte additive for high-rate all-solid-state lithium metal batteries. *ACS Appl. Mater. Interfaces* **2018**, *10*, 23874–23882.

[38] Xi, J. Y.; Qiu, X. P.; Cui, M. Z.; Tang, X. Z.; Zhu, W. T.; Chen, L. Q. Enhanced electrochemical properties of PEO-based composite polymer electrolyte with shape-selective molecular sieves. *J. Power Sources* **2006**, *156*, 581–588.

[39] Jamal, H.; Khan, F.; Hyun, S.; Min, S. W.; Kim, J. H. Enhancement of the ionic conductivity of a composite polymer electrolyte via surface functionalization of SSZ-13 zeolite for all-solid-state Li-metal batteries. *J. Mater. Chem. A* **2021**, *9*, 4126–4137.

[40] Yuan, C. F.; Li, J.; Han, P. F.; Lai, Y. Q.; Zhang, Z. A.; Liu, J. Enhanced electrochemical performance of poly(ethylene oxide) based composite polymer electrolyte by incorporation of nano-sized metal-organic framework. *J. Power Sources* **2013**, *240*, 653–658.

[41] Yu, J. M.; Guo, T. L.; Wang, C.; Shen, Z. H.; Dong, X. Y.; Li, S. H.; Zhang, H. G.; Lu, Z. D. Engineering two-dimensional metal-organic framework on molecular basis for fast Li^+ conduction. *Nano Lett.* **2021**, *21*, 5805–5812.

[42] Fu, X. W.; Hurlock, M. J.; Ding, C. F.; Li, X. Y.; Zhang, Q.; Zhong, W. H. MOF-enabled ion-regulating gel electrolyte for long-cycling lithium metal batteries under high voltage. *Small* **2022**, *18*, 2106225.

[43] Huo, H. Y.; Wu, B.; Zhang, T.; Zheng, X. S.; Ge, L.; Xu, T. W.; Guo, X. X.; Sun, X. L. Anion-immobilized polymer electrolyte achieved by cationic metal-organic framework filler for dendrite-free solid-state batteries. *Energy Stor. Mater.* **2019**, *18*, 59–67.

[44] Wang, H. C.; Wang, Q.; Cao, X.; He, Y. Y.; Wu, K.; Yang, J. J.; Zhou, H. H.; Liu, W.; Sun, X. M. Thiol-branched solid polymer electrolyte featuring high strength, toughness, and lithium ionic conductivity for lithium-metal batteries. *Adv. Mater.* **2020**, *32*, 2001259.

[45] Hu, Z. G.; Peng, Y. W.; Kang, Z. X.; Qian, Y. H.; Zhao, D. A modulated hydrothermal (MHT) approach for the facile synthesis of UiO-66-type MOFs. *Inorg. Chem.* **2015**, *54*, 4862–4868.

[46] Ameloot, R.; Aubrey, M.; Wiers, B. M.; Gómora-Figueroa, A. P.; Patel, S. N.; Balsara, N. P.; Long, J. R. Ionic conductivity in the metal-organic framework UiO-66 by dehydration and insertion of lithium *tert*-butoxide. *Chem.—Eur. J.* **2013**, *19*, 5533–5536.

[47] Ji, P. F.; Drake, T.; Murakami, A.; Oliveres, P.; Skone, J. H.; Lin, W. B. Tuning Lewis acidity of metal-organic frameworks via perfluorination of bridging ligands: Spectroscopic, theoretical, and catalytic studies. *J. Am. Chem. Soc.* **2018**, *140*, 10553–10561.

[48] Rey, I.; Lassègues, J. C.; Grondin, J.; Servant, L. Infrared and Raman study of the PEO-LiTFSI polymer electrolyte. *Electrochim. Acta* **1998**, *43*, 1505–1510.

[49] Yang, J. J.; Shao, L.; Wang, X.; Yang, Y.; Tian, Z. Y.; Chen, W. X.; Zhang, G.; Shen, C. Effect of intermolecular interactions on the performance of UiO-66-laden solid composite polymer electrolytes. *J. Alloys Compd.* **2020**, *845*, 155179.